Featured in Physics

Operating Semiconductor Qubits without Individual Barrier Gates

Alexander S. Ivlev,[1,*] Damien R. Crielaard,[1,*] Marcel Meyer,[1] William I. L. Lawrie,[1] Nico W. Hendrickx,[1] Amir Sammak,[2] Yuta Matsumoto,[1] Lieven M. K. Vandersypen,[1] Giordano Scappucci,[1] Corentin Déprez,[1] and Menno Veldhorst[1,†]

[1]*QuTech and Kavli Institute of Nanoscience, Delft University of Technology, PO Box 5046, 2600 GA Delft, The Netherlands*

[2]*QuTech and Netherlands Organisation for Applied Scientific Research (TNO), Delft, The Netherlands*

(Received 7 January 2025; revised 22 May 2025; accepted 24 June 2025; published 14 August 2025)

Semiconductor spin qubits have emerged as a promising platform for quantum computing, following a significant improvement in their control fidelities over recent years. Increasing the qubit count remains challenging, beginning with the fabrication of small features and complex fan-outs. A particular challenge has been formed by the need for individual barrier gates to control the exchange interaction between adjacent spin qubits. Here, we propose a method to vary two-qubit interactions without applying pulses on individual barrier gates while also remaining insensitive to detuning noise in first order. Experimentally we find that changing plunger gate voltages over 300 mV can tune the exchange energy J from 100 kHz to 60 MHz. This allows us to perform two-qubit operations without changing the barrier gate voltage. Based on these findings we conceptualize a spin qubit architecture without individual barrier gates, simplifying the fabrication while maintaining the control necessary for universal quantum computation.

DOI: 10.1103/xhq3-4jxz

Subject Areas: Condensed Matter Physics, Quantum Information, Semiconductor Physics

I. INTRODUCTION

A large qubit count is essential for achieving fault-tolerant quantum computing and quantum advantage. While various platforms are scaling to tens and even hundreds of qubits [1–4], a similar increase in the number of qubits with gate-defined quantum dots has remained challenging [5–7]. Even though their operational fidelities are competitive [8–11], and their scaling prospects are promising [12–14], the limited size of the current semiconductor spin systems so far prevents the platform to host meaningful quantum error correction experiments or large analog simulations [3,4,15–17]. The small array sizes moreover limit the ability to gather detailed statistics to improve the device designs, further slowing down the progress of the platform.

A key challenge in increasing the quantum dot array size is set by the small feature size of the quantum dot structures. The fabrication of these finer structures generally suffers in terms of resolution, uniformity, and yield, in particular when many need to be placed near one another. The introduction of hole spin devices in germanium has shown that increased feature sizes [18] can lead to the rapid growth of the quantum dot count, even in two dimensions [11,19–21]. Increasing the feature sizes may thus be a key step toward even larger quantum dot arrays, both for holes in germanium and for platforms where the charge carriers have a large effective mass, such as electrons and holes in silicon. It is therefore worth reconsidering the critical components of quantum dot devices necessary for future experiments. Current state-of-the-art devices [6,7,10,11,22] generally consist of individual plunger gates separated by dedicated barrier gates. Barrier gates in particular have a smaller footprint, making them more difficult to contact through vias and to fabricate. They are typically also more numerous as individual barrier gates are patterned in between each neighboring quantum dot pair. Thus, the use of individual barrier gates leads to a significant overhead, hindering the fabrication of larger arrays.

In this work, we take steps toward removing individual barrier gates, which are commonly used to tune the exchange interaction necessary for two-qubit gates. We introduce an alternative method to perform exchange operations without applying barrier gate pulses while staying at the charge symmetry point, where sensitivity

*These authors contributed equally to this work.

†Contact author: m.veldhorst@tudelft.nl

to charge noise is reduced. Instead, the exchange interaction can be altered by simultaneously increasing the chemical potential of two neighboring quantum dots. To increase the range of control of this method, two germanium quantum dots are isolated from the reservoir, allowing us to change their chemical potential by 10 times their charging energy. Notably, we see no significant decay in spin coherence over this large voltage range. In this regime, we show that our method allows us to vary the exchange interaction by more than 2 orders of magnitude, enabling the implementation of a controlled phase operation without pulsing on the barrier gate. Based on these findings, we propose a spin qubit architecture that does not rely on individual barrier gates.

II. METHODS TO TUNE THE EXCHANGE COUPLING

To eliminate barrier-based control of the exchange interaction, it is essential to understand the parameters that contribute to this exchange. The exchange energy $J \approx [4Ut_c^2/(U^2-\varepsilon^2)]$ between spins generally depends on the detuning ε between neighboring dots as well as the interdot tunnel coupling t_c [23]. Here $\varepsilon = 0$ corresponds to the charge symmetric point and $U \gg t_c$ is the on-site Coulomb interaction. In early experiments, the exchange interaction was manipulated using the detuning ε, as depicted in the simulated electrostatic potential of Fig. 1(a). This allows to control the exchange interaction in simple devices and it enabled pioneering work in the field [24–26]. However, due to the strong influence that detuning has on the exchange coupling at the interaction point, this method suffers from large charge noise susceptibility [27].

Noise resilience can be improved by staying at the symmetric charge sweet spot $\varepsilon = 0$, where J is to first order insensitive to noise on ε, and instead changing the tunnel coupling t_c (see Refs. [35,38] and the simulated fingerprint plot in Fig. 1(d)]. The tunnel coupling is commonly controlled using a dedicated barrier gate as depicted in Figs. 1(b) and 1(e) and it allows for high-fidelity two-qubit operations [8–11]. However, a third method can be envisioned, in which the tunnel coupling is controlled without changing the barrier gate voltage. Indeed, by simultaneously varying the chemical potential of both

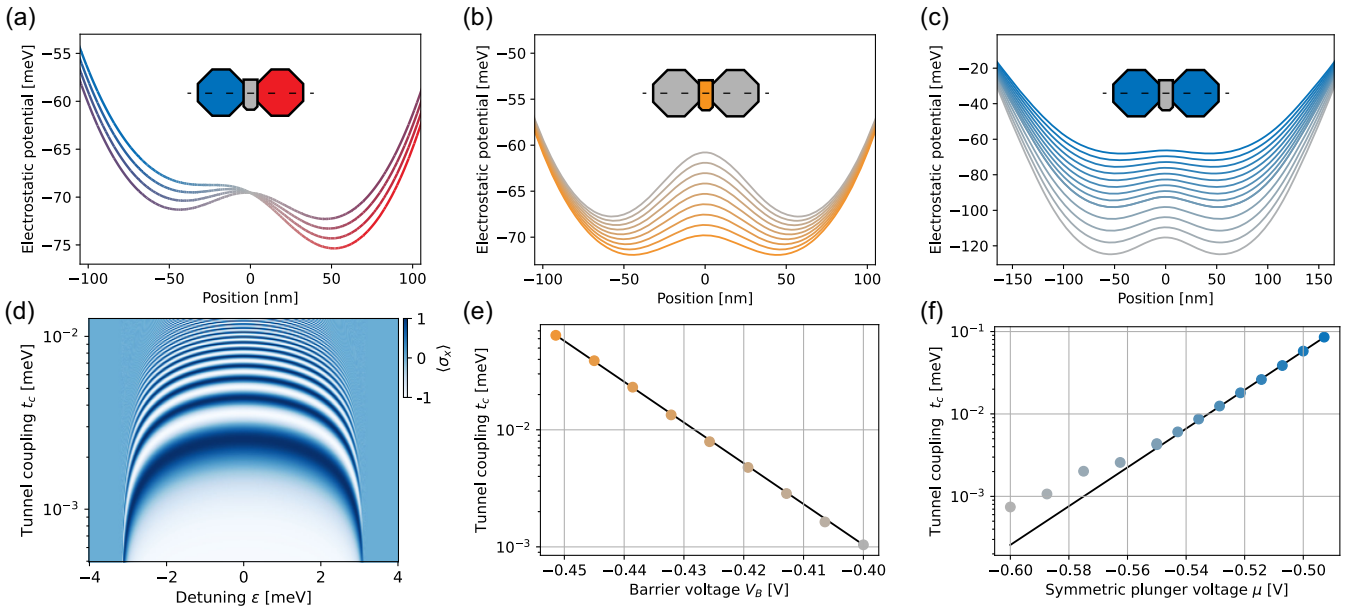

FIG. 1. Methods for manipulating the exchange coupling between spin qubits. (a) Simulated electrostatic potential in the quantum well when the detuning ε is varied to control the exchange coupling J. The inset depicts the device used during the simulation, as well as the dashed linecut along which the potential is plotted. The brighter colors correspond to larger detuning and thus larger exchange values. Details on the simulations performed can be found in Supplemental Material, Sec. I [28]. We note that to first order the tunnel coupling t_c does not change as ε is varied. (b) Simulated electrostatic potential when the barrier gate voltage V_B is used to control J through the tunnel coupling t_c. The line color corresponds to the voltage on the marker in (e) with the same color. The plunger gate voltages are fixed at $\mu = -0.5$ mV. (c) Simulated potential when the symmetric plunger voltage μ is used to control J through t_c, at $V_B = -0.45$ mV. The line color corresponds to the voltage on the marker (f) with the same color. (d) Simulated fingerprint plot [35] showing tunability of the exchange energy J when the tunnel coupling t_c and detuning ε are varied. The ensemble-average projection $\langle\sigma_x\rangle$ of a superposition state is depicted under the realistic assumptions of detuning noise and charging energy [36,37]. Details can be found in Supplemental Material I [28]. (e) Simulated t_c as function of V_B. The solid line is an exponential fit to the simulated data. (f) t_c is simulated as function of μ. Contrary to the barrier-based variation, the t_c does not have a pure exponential dependence with μ, which we hypothesize is related to the larger deformation of the confinement potential.

quantum dots μ as depicted in Fig. 1(c), one also changes the tunnel barrier and with it the exchange coupling, using only plunger gates. Crucially, t_c and thus J can be controlled this way while staying at the charge sweet spot $\varepsilon = 0$. We confirm this tunability of t_c in Fig. 1(f) with a Schrödinger-Poisson simulation with the Luttinger-Kohn Hamiltonian in QTCAD [39] (for details see Supplemental Material, Sec. I [28]). We will refer to this method of tuning t_c using μ as symmetric barrier-free pulsing.

III. OPERATING AN ISOLATED SPIN QUBIT PAIR

To study the symmetric barrier-free pulse scheme and compare it to the existing schemes, we use a Ge/SiGe qubit device with dedicated barrier gates between each plunger gate. This 2×2 quantum dot device, schematized in Fig. 2(a), and the underlying heterostructure have been introduced previously in, respectively, Refs. [5,40]. Details on the fabrication of the heterostructure and gate stack can be found in Supplemental Material, Sec. II [28]. The device has two single-hole transistors positioned diagonally across each other. During this experiment, the single-hole transistor next to plunger gate P_1 functions as both a charge sensor and a hole reservoir. Underneath plunger gates P_2 and P_3 we initialize a pair of hole spin qubits q_2 and q_3 in the $|\downarrow\downarrow\rangle$ state. While hole spins are used in this experiment, the underlying physics is understood to be the same for electrons, and the experiments can therefore be interpreted in the context of gate-defined quantum dot devices in general. Details on the readout and initialization can be found in Sec. VI. To control the exchange interaction J_{23} between the spins we change either the detuning $\varepsilon_{23} = \frac{1}{2}(vP_2 - vP_3)$, the virtualized barrier voltage vB_{23}, or the chemical potential on each quantum dot $\mu_{23} = \frac{1}{2}(vP_2 + vP_3)$. All gate voltages are virtualized to compensate for the crosstalk on the chemical potential of adjacent quantum dots [41]. We stress that this crosstalk is compensated with the corresponding plunger gate voltages and not the voltages on barrier gates B_{ij}. This means that when μ_{23} or ε_{23} are altered the voltage applied on the barrier

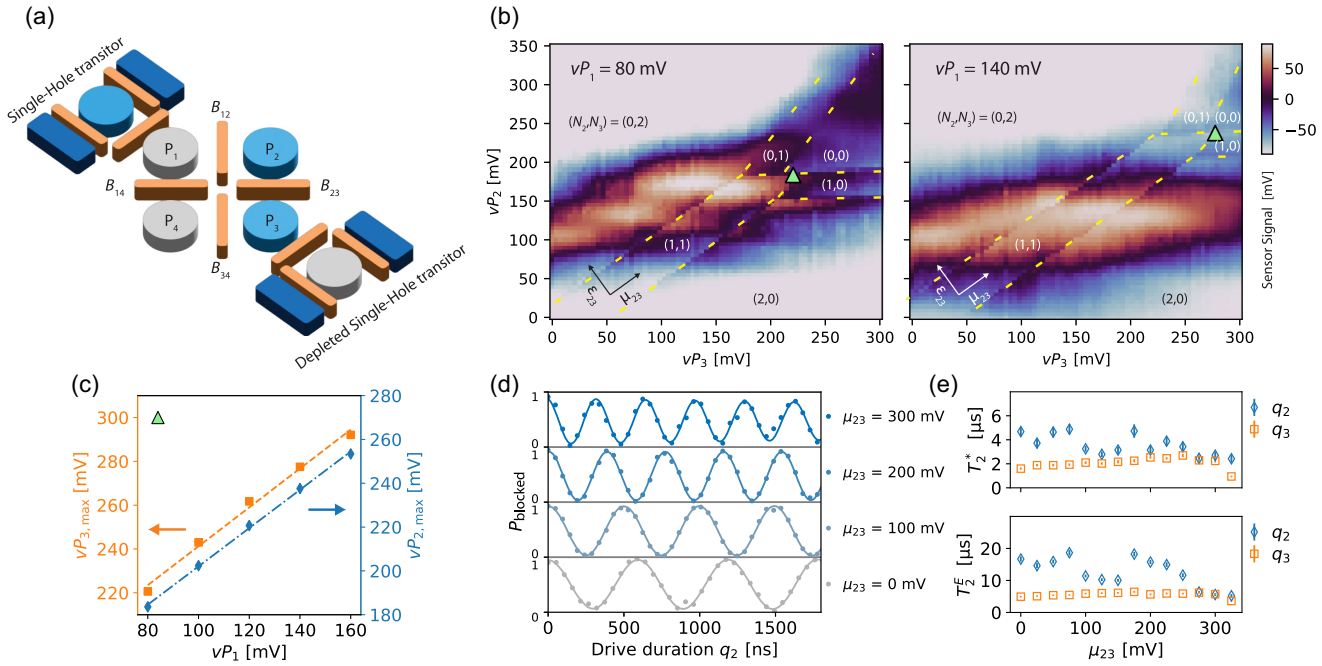

FIG. 2. Operating qubits in the isolated regime. (a) Schematic representation of the device used in this experiment. The blue color denotes the occupied quantum dots under P_2 and P_3, and the top single-hole transistor acts as a reservoir. The gray quantum dots under P_1, P_4, and the bottom single-hole transistor remain depleted. The dark blue elements are the Ohmic contacts and the various barrier gates are given in orange. The external magnetic field is fixed at $B_0 = 50$ mT approximately in plane, parallel to the line connecting P_2 and P_3. (b) Charge stability diagrams of the isolated two-hole regime using virtual plunger gates vP_2 and vP_3 for different values of vP_1. The detuning ϵ_{23} and chemical potential μ_{23} axes are indicated. The charge occupation (N_2, N_3) of quantum dots 2 and 3 is denoted in each charge region. The dashed lines serve as guide to the eye indicating charge transitions. For each quantum dot just two transitions are visible. The absence of additional charge transitions confirms the system is in the isolated regime. The maximal voltages $vP_{2,\max}$ and $vP_{3,\max}$ for which the quantum dots remain in a (1,1) occupation are marked by the green triangle. These voltages increase linearly with vP_1 as seen in (c), where the dashed lines indicate a linear fit of the maximal voltages as a function of vP_1. (d) Rabi oscillations induced by EDSR driving of q_2 at $\epsilon_{23} = 0$ for several values of μ_{23}. The solid line gives a fit to an exponentially decaying sinusoidal with visibilities up to 0.89 ± 0.01. (e) The Ramsey and Hahn-echo coherence times T_2^{*} and T_2^{E} as a function of μ_{23}, fitted using an exponentially decaying sine. The error bars give the standard deviation of the fitted coherence.

gates remains constant, and the pulse can be considered barrier-free as intended.

To avoid any spurious interactions and unwanted redistribution of charges, the quantum dots under P_1, under P_4, and the bottom single-hole transistor are depleted during operation [42–44]. This prevents any charges from loading onto or escaping from the quantum dots under P_2 and P_3 during operation through energetically favorable states on the neighboring sites. As a result, after the initial loading of two charges (see Sec. VI for loading sequence), no additional charges are loaded even after decreasing the chemical potential μ_{23} significantly. This is confirmed by the extended interdot transitions in the charge stability diagrams of Fig. 2(b). Moreover, the voltages at which charges are unloaded are dictated by the chemical potential of the neighboring quantum dots. Indeed, we see in Figs. 2(b) and 2(c) that the range over which the (1,1) charge state is maintained is linearly dependent on the voltage vP_1. Increasing the voltage on neighboring plunger gates therefore enlarges the range of μ_{23} that is applicable for the symmetric barrier-free operations. This isolation further ensures the absence of neighboring spins, preventing any spurious exchange interaction while varying the chemical potential. In the remainder of the presented data, the virtualized voltage on plunger gate 1 is set to $vP_1 =$ 240 mV. At this voltage, μ_{23} could be varied by roughly 350 mV while staying in the (1,1) charge state. This range corresponds to 10 times the charging voltage of 35 mV, as extracted from the charge stability diagrams. The dc voltages on the barrier gates B_{12}, B_{23}, B_{34} are set to be approximately −250 mV, mimicking the constraints of a global barrier architecture that is introduced later in the paper.

Given the accessible range of μ_{23}, we first check that the spin qubits remain coherent and can be operated after applying large voltage pulses on the plunger gates. We perform standard qubit characterization at different values of μ_{23} using Rabi, Ramsey, and Hahn-echo experiments. Some examples of Rabi oscillations obtained via electric dipole spin resonance (EDSR) driving at different values of μ_{23} are depicted in Fig. 2(d). Above $\mu_{23} = 325$ mV, Rabi oscillations started to degrade and EDSR driving was not possible. We hypothesize that this loss of EDSR signal at high μ_{23} results from a charge transition to the quantum dot underneath P_1. Having demonstrated the ability to drive the qubits, we characterize their coherence at different μ_{23} in Fig. 2(e). We do not observe a pronounced trend of the Ramsey (T_2^*) or Hahn-echo (T_2^E) coherence as a function of μ_{23}, apart from the coherence decrease at higher values which we attribute to an increased exchange coupling and with it a larger sensitivity to charge noise. The fact that coherence is generally maintained over such a large range in μ_{23} is encouraging for the symmetric barrier-free operation introduced here, as it suggests that a large tunability of the tunnel coupling can be achieved without undermining the individual qubit operation.

IV. CONTROLLING THE EXCHANGE

Now that the coherence of each individual qubit at varying μ_{23} is established, we can study the effect of μ_{23} on the exchange interaction between the two spins. We extract exchange oscillations using the sequence depicted in Fig. 3(a). Here the exchange interaction is turned on twice for a time $t_{\mathrm{exc}}/2$ with a double decoupling pulse in between [26,45]. This double decoupling pulse cancels out single-qubit phase accumulation induced by the exchange pulses, while the two-qubit conditional phase due to ZZ interactions is still being accumulated. Moreover, the decoupled sequence results in a longer coherence time of the state allowing us to probe smaller values of the exchange interaction J_{23} [46]. Using this technique we conduct a fingerprint scan [35] as a function of the virtual barrier voltage vB_{23} and detuning ε_{23} at a fixed total exchange time $t_{\mathrm{exc}} = 0.5$ μs. The resulting fingerprint plot can be found in Fig. 3(b). When the barrier gate voltage is decreased, more fringes appear due to the increasing exchange energy J_{23}, as we would expect from the simulated fingerprint in Fig. 1(d). We repeat this experiment, but varying μ_{23} instead of vB_{23} [Fig. 3(c)]. Crucially, now J_{23} increases when the voltage μ_{23} is increased, mirroring the dependence on vB_{23}. The fingerprint also confirms that we remain at the charge symmetry point as μ_{23} is swept along $\varepsilon_{23} = 0$. Similar to exchange pulses using dedicated barrier gates, it is therefore possible to keep low charge noise sensitivity while using only the plunger gates. We note that the feature around $\mu_{23} \approx 350$ mV coincides with the charge transition seen in the charge stability diagrams. Besides fingerprint plots, we further confirm the exchange tunability by studying the exchange splitting through EDSR measurements, which can be found in Supplemental Material, Sec. III [28]. Similar fingerprint plots are obtained for the quantum dot pair QD_1-QD_4 in Supplemental Material, Sec. IV [28].

To study the dependence of the exchange energy in more detail we vary the exchange time t_{exc} in the pulse sequence of Fig. 3(a) at $\epsilon_{23} = 0$. The time-resolved oscillations as a function of μ_{23} are shown in Fig. 3(d), with similar results for vB_{23}. The frequency of these oscillations equals $J_{23}/2$, which we extract by fitting a decaying sinusoid. In Fig. 3(e) we plot the extracted dependence of J_{23} on vB_{23} and μ_{23}. Over a large range of the barrier gate voltage, we see the expected exponential dependence of the exchange energy which is fitted to obtain a tunability of 36.6 ± 0.1 mV/dec, comparable to state-of-the-art devices [7]. We understand the apparent nonmonotonicity of J_{23} at higher values of vB_{23} to result from the level crossing of the singlet $|S\rangle$ and triplet $|T_-\rangle$ states (see Supplemental Material, Sec. III [28]). Moreover, we observe that J_{23} saturates at low values of $|\Delta V_B|$. Our method does not allow to extract lower exchange couplings considering the coherence times of our qubits. Looking at the symmetric barrier-free pulses, we see that changing μ_{23} allows us to tune J_{23} by

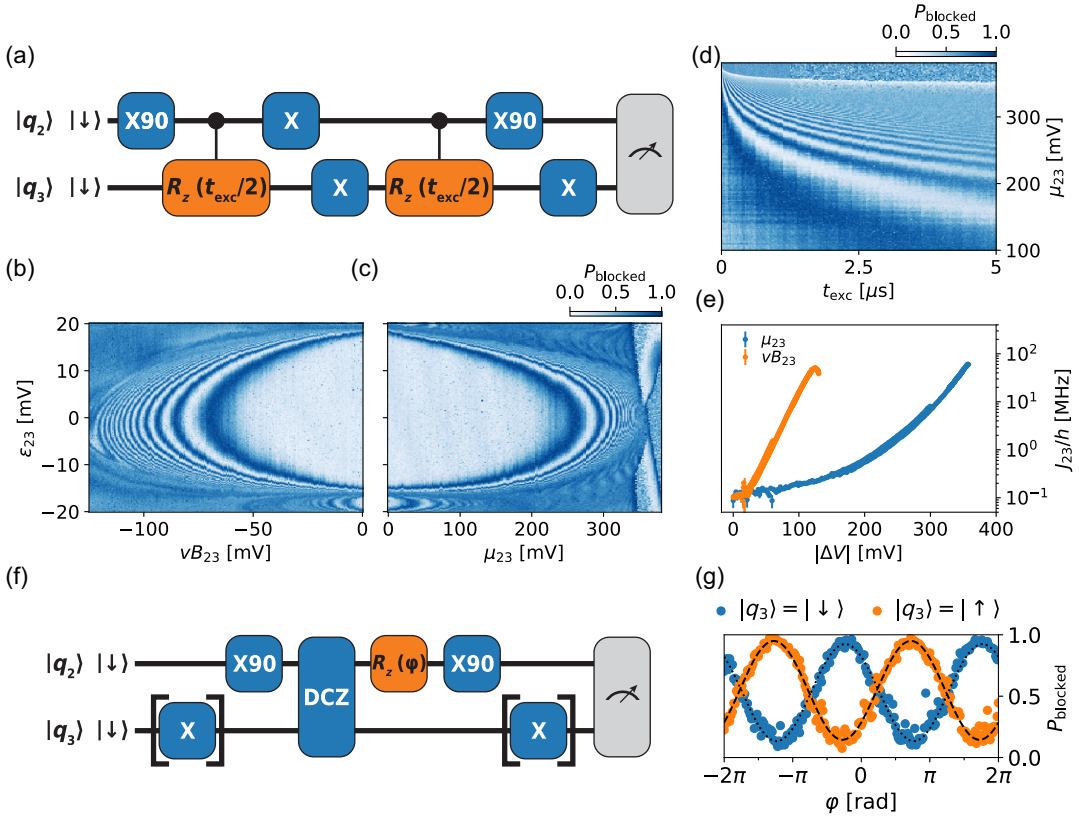

FIG. 3. Controlling exchange interaction with and without barrier gate pulses. (a) The gate sequence used to determine the exchange interaction J. q_2 is put into an equal spin superposition. The exchange is turned on during two controlled phase blocks, each lasting $t_{exc}/2$, separated by two decoupling pulses that cancel any single-qubit phase accumulation during the exchange pulse. Final single-qubit rotations allow for readout of distinguishable states. The blocks highlighted in orange are varied throughout (b)–(e). (b), (c) Fingerprint plots corresponding to the circuit in (a), where the exchange time is fixed at $t_{exc} = 0.5$ μs and the gate voltages are varied. The origin of both plots corresponds to the same voltage. (d) Exchange oscillations as a function of the exchange time t_{exc} at the symmetry point $\epsilon_{23} = 0$ mV. (e) Exchange energy J_{23} extracted from fitting the time-resolved oscillations in (d) and similar exchange oscillations induced by pulsing on the barrier gate. (f) The circuit used to demonstrate perform controlled-z pulses. q_2 is initialized in an equal spin superposition and an optional spin-flip is performed on q_3. The decoupled controlled-z (DCZ) pulse consists of two Tukey-window exchange pulses with a maximum height of $\mu_{23} = 275$ mV, separated by a double spin echo. To measure the phase of q_2 we perform a virtual rotation around the z axis, with varying phase φ. If q_3 was initialized in $|\uparrow\rangle$, it is flipped back for readout (see Sec. VI). (g) State evolution observed while implementing circuit (f). The oscillations obtained for an initial $q_3 = |\uparrow\rangle$ state are approximately π shifted compared to those obtained for an initial $q_3 = |\downarrow\rangle$ state, showing that the DCZ allows to perform a controlled-z operation.

approximately a factor of 600, from 100 kHz to 60 MHz. The maximal exchange reachable is limited by the available range of μ_{23} as discussed earlier. We further note that the exchange interaction does not follow an exponential dependence on μ_{23}. This is in line with the earlier simulation of tunnel coupling in Fig. 1(e), and we speculate that this results from a significant change in the confinement potential [see Fig. 1(c)]. To achieve the same maximum increase in effective exchange coupling, μ_{23} needs to be pulsed almost 3 times as much as the barrier gate voltage. We hypothesize this is partly explained by the barrier gate not only changing the potential barrier height but also its width, as seen in Fig. 1(b). Moreover, this difference could result from the higher lever arm of vB_{23} compared to that of the plunger gates, as the former is fabricated in a lower gate layer [5]. Given the limited swing of an arbitrary waveform generator, increasing the lever arm of the plunger gates would in general allow us to more effectively isolate the system and enlarge the range over which μ_{23} can be pulsed. In future devices, the plunger gates can be fabricated at a lower gate layer to gain these benefits. Already in the current device, however, the range of μ_{23} is large enough to access similar values of the exchange energy as with the dedicated barrier gate, and achieve on-off ratios comparable to the state-of-the-art devices [6,9,47].

In the current experiment, the quality of the exchange oscillation is higher for the barrier-based pulses with up to $Q_{B_{23}} = 20 \pm 2$ compared to the symmetric barrier-free exchange oscillation $Q_{\mu_{23}} = 10 \pm 2$, while we find that the QD_1-QD_4 pair has $Q_{\mu_{14}} = 18 \pm 4$ (see Supplemental

Material, Sec. V [28] for details). The variation in the barrier-free quality factor may come from the specific potential landscape and charge noise present.

By controlling the exchange energy with symmetric barrier-free pulses it is possible to realize state-dependent interactions without pulsing on dedicated barrier gates. We use this to demonstrate a decoupled controlled-Z operation between q_2 and q_3 after preparing q_2 in an equal superposition [Fig. 3(f)]. For each exchange pulse, we pulse to $\mu_{23} = 275$ mV using a Tukey window [9,11,48] to enhance adiabaticity. After the two-qubit operation, we study the state-dependent phase accumulation, with the result depicted in Fig. 3(g). After the decoupled exchange pulse, the superposition state of q_2 gains a relative phase of $(1.041 \pm 0.006)\pi$ when q_3 is flipped, as is expected from a controlled-Z pulse.

V. MERGED GRID ARCHITECTURE

Having shown the ability to perform entangling operations without using a dedicated barrier, we incorporate this technique into an architecture design for large-scale semiconductor quantum processors. In this architecture, the numerous barrier gates are merged into a large two-dimensional barrier grid, as schematically depicted in Fig. 4. The plunger gates are still separately connected to allow for individual control over the chemical potential of each quantum dot. The array is generally sparsely occupied, with the spin qubits brought together only during two-qubit operations, initialization, and readout. The sparse occupation enables the use of the symmetric barrier-free pulses investigated here without creating spurious interactions.

In this architecture, the global barrier grid helps to confine a spin to a single quantum dot and coarsely sets the tunnel coupling between adjacent quantum dots, while control over each individual plunger gate enables universal

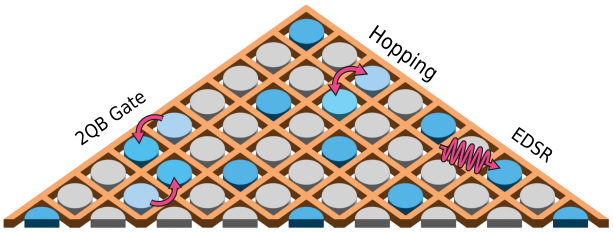

FIG. 4. Merged barrier architecture and operation. A clipped section of the proposed scalable quantum dot array architecture. The individual barrier gates are merged into a single barrier grid (orange). The quantum dots are sparsely occupied (blue). The empty quantum dots (gray) can be used to connect distant qubits or provide space for qubit operation. The exact choice of occupation generally depends on the desired functionality of the empty quantum dots. Charge sensors can be integrated within the array itself or placed on the periphery. Arrows indicate possible operations like EDSR, hopping-based single-qubit gates and two-qubit (2QB) gates through shuttling.

qubit operation. Single-qubit gates can be performed through EDSR, or through spin hopping [11]. Two-qubit gates are executed by moving two spins together and performing the symmetric barrier-free operations demonstrated in this paper. We emphasize that the symmetric, detuning-insensitive aspect of this method allows the global barrier grid to be a viable alternative to individual barrier gate control. Two-qubit gates can be further tuned by varying the time that qubits spend adjacent to each other. Finally, while this paper focused on controlling the exchange interaction, it is expected that initialization and readout can be achieved without individual barrier control in a similar fashion (see the discussion in Sec. VI). Symmetric barrier-free pulses can again be used to tune the tunnel coupling to the values desired for high-fidelity initialization and readout [22,49].

To have full control over each physical qubit, the number of electronic connections still grows linearly with the number of qubits in this merged barrier architecture. Yet, with the removal of individual barrier gates, the distance between leads is increased. This increase of effective footprint simplifies the local fan-out significantly. Moreover, since plunger gates are typically larger than barrier gates, these remaining plunger gates are easier to contact using vias. These simplifications could allow spin-qubit array sizes to increase in two dimensions more easily, which is valuable for fault-tolerant computation [3,4].

We further note that the sparse occupation required results in an additional overhead compared to a dense occupation. This is deemed acceptable given the functionalities a sparse architecture provides, like integrated shuttling lanes [50–53] for increased connectivity to support efficient error correction [54], space for high-fidelity hopping-based gates [11,55], and reduced crosstalk due to increased qubit spacing [56]. Still, a dense occupation of the quantum dot array is conceivable in the context of analog quantum simulation experiments, where the global barrier grid allows us to turn on all interactions between the neighboring quantum dots simultaneously, albeit with some natural variability. This architecture would then allow quantum dot experiments [57,58] to more readily reach the sizes for analog simulation that have been achieved in atomic and superconducting systems [15–17].

In conclusion, we have investigated the effect of symmetrically pulsing on both plunger gates of a double quantum dot. We have seen that in an isolated regime, these pulses do not significantly limit qubit coherence, providing an additional control parameter for quantum dot operation. Using these symmetric pulses we can tune the exchange interaction over 2 orders of magnitude, limited by the attainable voltage range and the lever arm of the plunger gates. By optimizing the gate stack to increase the lever arm of the plunger gates, the exchange tunability can be further enhanced in future devices. The currently available control still allows to implement a decoupled CZ two-qubit gate

without pulsing on the barrier gate. These results enable the introduction of an architecture that does not rely on individual barrier gates, while crucially maintaining universal quantum control at a detuning-insensitive operating point. Consequently, the small barrier gates of current semiconductor quantum processors can be merged into a grid in future designs, facilitating scaling toward the sizes needed for useful quantum simulation and computation.

VI. METHODS

A. Initialization and readout

At the beginning of each experimental shot, two hole spins are loaded onto quantum dot 1 from the reservoir. After loading, the tunnel coupling to the reservoir is decreased and the spins are shuttled from quantum dot 1 to quantum dot 2, where they are in a spin singlet. Through adiabatic transfer from the (0,2,0,0) to the (0,1,1,0) charge state, the $|\downarrow\downarrow\rangle$ spin state is formed in quantum dots 2 and 3. Figure 5(a) shows the schematic of this initialization process. During the loading and initialization, the voltages on virtual barrier gates vB_{23} and vB_{34} are pulsed by -40 and -50 mV, respectively. Similar pulses are applied during the readout sequence described later. Considering the exchange tunability achieved with the barrier-free operation, we believe that symmetric barrier-free pulses can provide sufficient control over the tunnel coupling to initialize without using individual barrier gates. In particular, we observe in Fig. 3(e) that μ can be used to realize the same exchange variation as a 125 mV pulse on the barrier gate. As a result, we foresee that in future work the entire qubit experiment can be performed without pulsing on the local barrier gate at all.

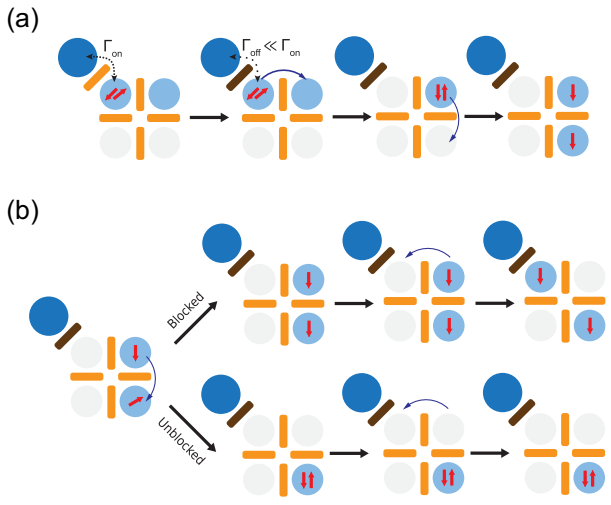

FIG. 5. Schematics of the qubit initialisation and readout. (a) For initialization, spins are loaded from the reservoir and shuttled to the active quantum dots. After loading, the tunnel rate Γ to the reservoir is decreased. (b) For spin readout, after performing spin-to-charge conversion, any existing charge under plunger gate P_2 is shuttled to the charge sensor for readout.

Spin readout starts with spin-to-charge conversion through Pauli spin blockade. This allows us to distinguish between singlet and triplet states. In our readout routine the $|\downarrow\downarrow\rangle$ basis state is mapped to the unblocked singlet, while the other states are blocked [59]. Therefore, to probe the dynamics of either spin state, we make sure the other spin state is $|\downarrow\rangle$. Following spin-to-charge conversion, we perform a charge shuttling step to enhance the charge signal during readout. After Pauli spin blockade between quantum dots 2 and 3, the unblocked spins lead to the (0,0,2,0) charge occupancy while the blocked charge state is still in the (0,1,1,0) occupancy. We lower the voltage on plunger gate 1 to allow any charges in quantum dot 2 to shuttle there. The (0,1,1,0) state becomes the (1,0,1,0), while the (0,0,2,0) is unchanged. This charge state difference is picked up by the charge sensors to determine the initial spin state. A schematic of this spin-to-charge conversion can be found in Fig. 5(b).

Each presented data point typically corresponds to $N_{\text{shots}} = 300$ shots. The threshold to classify the sensor signal into blocked or unblocked states was put in the middle between the maximal and minimum values measured during these N_{shots}.

ACKNOWLEDGMENTS

We thank Sander de Snoo for continuous software development, and Olaf Benningshof and Chien-An Wang for maintenance and support of the experimental setup. We thank Francesco Borsoi for fruitful discussions. We acknowledge support by the Dutch Research Council through an NWO ENW grant and by the Dutch National Growth Fund (NGF), as part of the Quantum Delta NL program. We acknowledge the European Union through ERC Starting Grant QUIST (No. 850641) and through the IGNITE project of European Union's Horizon Europe Framework Programme under Grant Agreement No. 101069515. This research was sponsored in part by the Army Research Office (ARO) under Award No. W911NF-23-1-0110.

A. S. I. is an inventor on a patent application on the merged barrier architecture filed by Delft University of Technology under the application No. NL38924. N. W. H. is a founder, and M. V., G. S. and L. M. K. V. are founding advisors of Groove Quantum BV, with N. W. H., M. V., G. S., and L. M. K. V. declaring equity interests. The remaining authors declare that they have no competing interests.

The views, conclusions, and recommendations contained in this document are those of the authors and are not necessarily endorsed nor should they be interpreted as representing the official policies, either expressed or implied, of the Army Research Office (ARO) or the

DATA AVAILABILITY

The data that support the findings of this article are openly available [60].

[1] Y. Kim, A. Eddins, S. Anand, K. X. Wei, E. van den Berg, S. Rosenblatt, H. Nayfeh, Y. Wu, M. Zaletel, K. Temme, and A. Kandala, *Evidence for the utility of quantum computing before fault tolerance*, Nature (London) **618**, 500 (2023).

[2] M. DeCross *et al.*, *Computational power of random quantum circuits in arbitrary geometries*, Phys. Rev. X **15**, 021052 (2025).

[3] D. Bluvstein *et al.*, *Logical quantum processor based on reconfigurable atom arrays*, Nature (London) **626**, 58 (2024).

[4] R. Acharya *et al.* (Google Quantum AI and Collaborators), *Quantum error correction below the surface code threshold*, Nature (London) **638**, 920 (2025).

[5] N. W. Hendrickx, W. I. L. Lawrie, M. Russ, F. van Riggelen, S. L. de Snoo, R. N. Schouten, A. Sammak, G. Scappucci, and M. Veldhorst, *A four-qubit germanium quantum processor*, Nature (London) **591**, 580 (2021).

[6] S. G. J. Philips, M. T. Mądzik, S. V. Amitonov, S. L. De Snoo, M. Russ, N. Kalhor, C. Volk, W. I. L. Lawrie, D. Brousse, L. Tryputen, B. P. Wuetz, A. Sammak, M. Veldhorst, G. Scappucci, and L. M. K. Vandersypen, *Universal control of a six-qubit quantum processor in silicon*, Nature (London) **609**, 919 (2022).

[7] H. C. George *et al.*, *12-spin-qubit arrays fabricated on a 300 mm semiconductor manufacturing line*, Nano Lett. **25**, 793 (2025).

[8] A. Noiri, K. Takeda, T. Nakajima, T. Kobayashi, A. Sammak, G. Scappucci, and S. Tarucha, *Fast universal quantum gate above the fault-tolerance threshold in silicon*, Nature (London) **601**, 338 (2022).

[9] X. Xue, M. Russ, N. Samkharadze, B. Undseth, A. Sammak, G. Scappucci, and L. M. K. Vandersypen, *Quantum logic with spin qubits crossing the surface code threshold*, Nature (London) **601**, 343 (2022).

[10] A. R. Mills, C. R. Guinn, M. J. Gullans, A. J. Sigillito, M. M. Feldman, E. Nielsen, and J. R. Petta, *Two-qubit silicon quantum processor with operation fidelity exceeding 99%*, Sci. Adv. **8**, eabn5130 (2022).

[11] C.-A. Wang, V. John, H. Tidjani, C. X. Yu, A. S. Ivlev, C. Déprez, F. Van Riggelen-Doelman, B. D. Woods, N. W. Hendrickx, W. I. L. Lawrie, L. E. A. Stehouwer, S. D. Oosterhout, A. Sammak, M. Friesen, G. Scappucci, S. L. De Snoo, M. Rimbach-Russ, F. Borsoi, and M. Veldhorst, *Operating semiconductor quantum processors with hopping spins*, Science **385**, 447 (2024).

[12] A. M. J. Zwerver *et al.*, *Qubits made by advanced semiconductor manufacturing*, Nat. Electron. **5**, 184 (2022).

[13] S. Neyens *et al.*, *Probing single electrons across 300-mm spin qubit wafers*, Nature (London) **629**, 80 (2024).

[14] P. Steinacker *et al.*, *A 300 mm foundry silicon spin qubit unit cell exceeding 99% fidelity in all operations*, arXiv: 2410.15590.

[15] I. Bloch, J. Dalibard, and S. Nascimbène, *Quantum simulations with ultracold quantum gases*, Nat. Phys. **8**, 267 (2012).

[16] P. Scholl, M. Schuler, H. J. Williams, A. A. Eberharter, D. Barredo, K.-N. Schymik, V. Lienhard, L.-P. Henry, T. C. Lang, T. Lahaye, A. M. Läuchli, and A. Browaeys, *Quantum simulation of 2D antiferromagnets with hundreds of Rydberg atoms*, Nature (London) **595**, 233 (2021).

[17] A. H. Karamlou, I. T. Rosen, S. E. Muschinske, C. N. Barrett, A. Di Paolo, L. Ding, P. M. Harrington, M. Hays, R. Das, D. K. Kim, B. M. Niedzielski, M. Schuldt, K. Serniak, M. E. Schwartz, J. L. Yoder, S. Gustavsson, Y. Yanay, J. A. Grover, and W. D. Oliver, *Probing entanglement in a 2D hard-core Bose-Hubbard lattice*, Nature (London) **629**, 561 (2024).

[18] M. Lodari, A. Tosato, D. Sabbagh, M. A. Schubert, G. Capellini, A. Sammak, M. Veldhorst, and G. Scappucci, *Light effective hole mass in undoped* Ge/SiGe *quantum wells*, Phys. Rev. B **100**, 041304(R) (2019).

[19] N. W. Hendrickx, D. P. Franke, A. Sammak, M. Kouwenhoven, D. Sabbagh, L. Yeoh, R. Li, M. L. V. Tagliaferri, M. Virgilio, G. Capellini, G. Scappucci, and M. Veldhorst, *Gate-controlled quantum dots and superconductivity in planar germanium*, Nat. Commun. **9**, 2835 (2018).

[20] F. van Riggelen, N. W. Hendrickx, W. I. L. Lawrie, M. Russ, A. Sammak, G. Scappucci, and M. Veldhorst, *A two-dimensional array of single-hole quantum dots*, Appl. Phys. Lett. **118**, 044002 (2021).

[21] F. Borsoi, N. W. Hendrickx, V. John, M. Meyer, S. Motz, F. van Riggelen, A. Sammak, S. L. de Snoo, G. Scappucci, and M. Veldhorst, *Shared control of a 16 semiconductor quantum dot crossbar array*, Nat. Nanotechnol. **19**, 21 (2024).

[22] K. Takeda, A. Noiri, T. Nakajima, L. C. Camenzind, T. Kobayashi, A. Sammak, G. Scappucci, and S. Tarucha, *Rapid single-shot parity spin readout in a silicon double quantum dot with fidelity exceeding 99%*, npj Quantum Inf. **10**, 1 (2024).

[23] G. Burkard, T. D. Ladd, A. Pan, J. M. Nichol, and J. R. Petta, *Semiconductor spin qubits*, Rev. Mod. Phys. **95**, 025003 (2023).

[24] J. R. Petta, A. C. Johnson, J. M. Taylor, E. A. Laird, A. Yacoby, M. D. Lukin, C. M. Marcus, M. P. Hanson, and A. C. Gossard, *Coherent manipulation of coupled electron spins in semiconductor quantum dots*, Science **309**, 2180 (2005).

[25] M. Veldhorst, C. H. Yang, J. C. C. Hwang, W. Huang, J. P. Dehollain, J. T. Muhonen, S. Simmons, A. Laucht, F. E. Hudson, K. M. Itoh, A. Morello, and A. S. Dzurak, *A two-qubit logic gate in silicon*, Nature (London) **526**, 410 (2015).

[26] T. F. Watson, S. G. J. Philips, E. Kawakami, D. R. Ward, P. Scarlino, M. Veldhorst, D. E. Savage, M. G. Lagally, M. Friesen, S. N. Coppersmith, M. A. Eriksson, and L. M. K. Vandersypen, *A programmable two-qubit quantum processor in silicon*, Nature (London) **555**, 633 (2018).

[27] O. E. Dial, M. D. Shulman, S. P. Harvey, H. Bluhm, V. Umansky, and A. Yacoby, *Charge noise spectroscopy using coherent exchange oscillations in a singlet-triplet qubit*, Phys. Rev. Lett. **110**, 146804 (2013).

[28] See Supplemental Material at http://link.aps.org/supplemental/10.1103/xhq3-4jxz, which includes Refs. [29–34], for additional details about the device and numerical simulations as well as further analysis of experimental data. Sections (I) for details about the simulation, (II) for details on the device and fabrication, (III) for experimental data where EDSR spectroscopy is used to further study the exchange interaction, (IV) for data on the quantum dot pair QD1 and QD4, (V) for analysis on the quality of the exchange oscillations.

[29] V. John, F. Borsoi, Z. György, C.-A. Wang, G. Széchenyi, F. van Riggelen-Doelman, W. I. L. Lawrie, N. W. Hendrickx, A. Sammak, G. Scappucci, A. Pályi, and M. Veldhorst, *Bichromatic Rabi control of semiconductor qubits*, Phys. Rev. Lett. **132**, 067001 (2024).

[30] D. Stepanenko, M. Rudner, B. I. Halperin, and D. Loss, *Singlet-triplet splitting in double quantum dots due to spin-orbit and hyperfine interactions*, Phys. Rev. B **85**, 075416 (2012).

[31] D. Jirovec, A. Hofmann, A. Ballabio, P. M. Mutter, G. Tavani, M. Botifoll, A. Crippa, J. Kukucka, O. Sagi, F. Martins, J. Saez-Mollejo, I. Prieto, M. Borovkov, J. Arbiol, D. Chrastina, G. Isella, and G. Katsaros, *A singlet-triplet hole spin qubit in planar Ge*, Nat. Mater. **20**, 1106 (2021).

[32] J. Saez-Mollejo, D. Jirovec, Y. Schell, J. Kukucka, S. Calcaterra, D. Chrastina, G. Isella, M. Rimbach-Russ, S. Bosco, and G. Katsaros, *Exchange anisotropies in microwave-driven singlet-triplet qubits*, Nat. Commun. **16**, 3862 (2025).

[33] M. T. Mądzik *et al.*, *Operating two exchange-only qubits in parallel*, arXiv:2504.01191.

[34] P. Stano and D. Loss, *Review of performance metrics of spin qubits in gated semiconducting nanostructures*, Nat. Rev. Phys. **4**, 672 (2022).

[35] M. D. Reed, B. M. Maune, R. W. Andrews, M. G. Borselli, K. Eng, M. P. Jura, A. A. Kiselev, T. D. Ladd, S. T. Merkel, I. Milosavljevic, E. J. Pritchett, M. T. Rakher, R. S. Ross, A. E. Schmitz, A. Smith, J. A. Wright, M. F. Gyure, and A. T. Hunter, *Reduced sensitivity to charge noise in semiconductor spin qubits via symmetric operation*, Phys. Rev. Lett. **116**, 110402 (2016).

[36] N. W. Hendrickx, L. Massai, M. Mergenthaler, F. J. Schupp, S. Paredes, S. W. Bedell, G. Salis, and A. Fuhrer, *Sweet-spot operation of a germanium hole spin qubit with highly anisotropic noise sensitivity*, Nat. Mater. **23**, 920 (2024).

[37] L. E. A. Stehouwer, C. X. Yu, B. van Straaten, A. Tosato, V. John, D. Degli Esposti, A. Elsayed, D. Costa, S. D. Oosterhout, N. W. Hendrickx, M. Veldhorst, F. Borsoi, and G. Scappucci, *Exploiting strained epitaxial germanium for scaling low-noise spin qubits at the micrometre scale*, Nat. Mater. (2025), 10.1038/s41563-025-02276-w.

[38] F. Martins, F. K. Malinowski, P. D. Nissen, E. Barnes, S. Fallahi, G. C. Gardner, M. J. Manfra, C. M. Marcus, and F. Kuemmeth, *Noise Suppression using symmetric exchange gates in spin qubits*, Phys. Rev. Lett. **116**, 116801 (2016).

[39] QTCAD/Assisted Design for Quantum Technologies | Nanoacademic, https://nanoacademic.com/solutions/qtcad/.

[40] M. Lodari, N. W. Hendrickx, W. I. L. Lawrie, T.-K. Hsiao, L. M. K. Vandersypen, A. Sammak, M. Veldhorst, and G. Scappucci, *Low percolation density and charge noise with holes in germanium*, Mater. Quantum Technol. **1**, 011002 (2021).

[41] T. Hensgens, T. Fujita, L. Janssen, X. Li, C. J. Van Diepen, C. Reichl, W. Wegscheider, S. Das Sarma, and L. M. K. Vandersypen, *Quantum simulation of a Fermi-Hubbard model using a semiconductor quantum dot array*, Nature (London) **548**, 70 (2017).

[42] H. G. J. Eenink, L. Petit, W. I. L. Lawrie, J. S. Clarke, L. M. K. Vandersypen, and M. Veldhorst, *Tunable coupling and isolation of single electrons in silicon metal-oxide-semiconductor quantum dots*, Nano Lett. **19**, 8653 (2019).

[43] T. Tanttu *et al.*, *Assessment of the errors of high-fidelity two-qubit gates in silicon quantum dots*, Nat. Phys. **20**, 1804 (2024).

[44] B. Bertrand, H. Flentje, S. Takada, M. Yamamoto, S. Tarucha, A. Ludwig, A. D. Wieck, C. Bäuerle, and T. Meunier, *Quantum manipulation of two-electron spin states in isolated double quantum dots*, Phys. Rev. Lett. **115**, 096801 (2015).

[45] M. Russ, D. M. Zajac, A. J. Sigillito, F. Borjans, J. M. Taylor, J. R. Petta, and G. Burkard, *High-fidelity quantum gates in* Si/SiGe *double quantum dots*, Phys. Rev. B **97**, 085421 (2018).

[46] N. Wang, S.-M. Wang, R.-Z. Zhang, J.-M. Kang, W.-L. Lu, H.-O. Li, G. Cao, B.-C. Wang, and G.-P. Guo, *Pursuing high-fidelity control of spin qubits in natural* Si/SiGe *quantum dot*, Appl. Phys. Lett. **125**, 204002 (2024).

[47] A. J. Weinstein *et al.*, *Universal logic with encoded spin qubits in silicon*, Nature (London) **615**, 817 (2023).

[48] M. Rimbach-Russ, S. G. J. Philips, X. Xue, and L. M. K. Vandersypen, *Simple framework for systematic high-fidelity gate operations*, Quantum Sci. Technol. **8**, 045025 (2023).

[49] M. Nurizzo, B. Jadot, P.-A. Mortemousque, V. Thiney, E. Chanrion, D. Niegemann, M. Dartiailh, A. Ludwig, A. D. Wieck, C. Bäuerle, M. Urdampilleta, and T. Meunier, *Complete readout of two-electron spin states in a double quantum dot*, PRX Quantum **4**, 010329 (2023).

[50] I. Seidler, T. Struck, R. Xue, N. Focke, S. Trellenkamp, H. Bluhm, and L. R. Schreiber, *Conveyor-mode single-electron shuttling in* Si/SiGe *for a scalable quantum computing architecture*, npj Quantum Inf. **8**, 1 (2022).

[51] A. M. J. Zwerver, S. V. Amitonov, S. L. De Snoo, M. T. Mądzik, M. Rimbach-Russ, A. Sammak, G. Scappucci, and L. M. K. Vandersypen, *Shuttling an electron spin through a silicon quantum dot array*, PRX Quantum **4**, 030303 (2023).

[52] M. Künne, A. Willmes, M. Oberländer, C. Gorjaew, J. D. Teske, H. Bhardwaj, M. Beer, E. Kammerloher, R. Otten, I. Seidler, R. Xue, L. R. Schreiber, and H. Bluhm, *The SpinBus architecture for scaling spin qubits with electron shuttling*, Nat. Commun. **15**, 4977 (2024).

[53] F. van Riggelen-Doelman, C.-A. Wang, S. L. de Snoo, W. I. L. Lawrie, N. W. Hendrickx, M. Rimbach-Russ, A. Sammak, G. Scappucci, C. Déprez, and M. Veldhorst, *Coherent spin qubit shuttling through germanium quantum dots*, Nat. Commun. **15**, 5716 (2024).

[54] S. Bravyi, A. W. Cross, J. M. Gambetta, D. Maslov, P. Rall, and T. J. Yoder, *High-threshold and low-overhead fault-tolerant quantum memory*, Nature (London) **627**, 778 (2024).

[55] F. K. Unseld, B. Undseth, E. Raymenants, Y. Matsumoto, S. L. de Snoo, S. Karwal, O. Pietx-Casas, A. S. Ivlev, M. Meyer, A. Sammak, M. Veldhorst, G. Scappucci, and L. M. K. Vandersypen, *Baseband control of single-electron silicon spin qubits in two dimensions*, Nat. Commun. **16**, 5605 (2025).

[56] V. John, C. X. Yu, B. van Straaten, E. A. Rodríguez-Mena, M. Rodríguez, S. Oosterhout, L. E. A. Stehouwer, G. Scappucci, S. Bosco, M. Rimbach-Russ, Y.-M. Niquet, F. Borsoi, and M. Veldhorst, *A two-dimensional 10-qubit array in germanium with robust and localised qubit control*, arXiv:2412.16044.

[57] C. J. van Diepen, T.-K. Hsiao, U. Mukhopadhyay, C. Reichl, W. Wegscheider, and L. M. K. Vandersypen, *Quantum simulation of antiferromagnetic Heisenberg chain with gate-defined quantum dots*, Phys. Rev. X **11**, 041025 (2021).

[58] C.-A. Wang, C. Déprez, H. Tidjani, W. I. L. Lawrie, N. W. Hendrickx, A. Sammak, G. Scappucci, and M. Veldhorst, *Probing resonating valence bonds on a programmable germanium quantum simulator*, npj Quantum Inf. **9**, 1 (2023).

[59] E. G. Kelly, L. Massai, B. Hetényi, M. Pita-Vidal, A. Orekhov, C. Carlsson, I. Seidler, K. Tsoukalas, L. Sommer, M. Aldeghi, S. W. Bedell, S. Paredes, F. J. Schupp, M. Mergenthaler, A. Fuhrer, G. Salis, and P. Harvey-Collard, *Identifying and mitigating errors in hole spin qubit readout*, arXiv:2504.06898.

[60] A. Ivlev *et al.*, Scripts and Data for: "Operating semiconductor qubits without individual barrier gates", Zenodo (2025), 10.5281/zenodo.15829323.